



# Three-dimensional modeling of fluid dynamics and heat transfer for two-fluid or phase change flows



Yeng-Yung Tsui\*, Shi-Wen Lin

Department of Mechanical Engineering, National Chiao Tung University, Hsinchu 300, Taiwan, ROC

## ARTICLE INFO

### Article history:

Received 3 February 2015

Received in revised form 5 September 2015

Accepted 8 September 2015

Available online 24 October 2015

### Keywords:

Two-phase flow

Phase change

Heat transfer

Interface tracking

VOF method

## ABSTRACT

A numerical algorithm based on the VOF method was proposed to solve two-phase/two-fluid flow problems by the authors recently. Different from other surface reconstruction approaches, the interface between the two fluids is represented by a continuous surface as the contour surface of the VOF function. It is robust and easy to implement. In this article, the method is extended to deal with three-dimensional flows. Also considered in the study is the heat transfer in the flow with or without phase change. In order to validate the method, a variety of flow problems are under consideration and comparison with empirical correlations is made. The method is first tested by considering a benchmark case with prescribed 3-D velocity field. It is then applied to the problem of bubble rising in a quiescent liquid, followed by investigating the splashing of a drop impacting on a liquid film. To assess the heat transfer model for phase change, the boiling flow emerging from a superheated planar film is under investigation. The last one considered is a jet flow caused by injection of high-temperature octane into a water container.

© 2015 Elsevier Ltd. All rights reserved.

## 1. Introduction

Two-phase/two fluid flows can be found in a variety of applications in industrial processes. Earlier studies on this subject heavily rely on experiments. The fast advancement in numerical techniques has made accurate simulation of these flows feasible in the past two decades. Unlike single-fluid flows, there is an interface between the two fluids across which thermophysical properties suffer significant changes, making the mathematical problem more stiff to be solved. The situation becomes even worse by understanding that the position of the interface requires to be solved as part of the solution.

To solve the multi-fluid problems, a widely adopted approach is to treat the fluids as a single fluid with variable thermal properties and use an Eulerian grid to allow the interface to move around in the grid. Therefore, one of the most important issues in this modeling is to track the interface accurately. Owing to the jump of the thermal properties, the methods similar to the shock-capturing schemes employed in high-speed, compressible flows will inherently suffer diffusion at the fluid surface [1,2]. To avoid this problem, various methods have been developed. In the front tracking method [3–5], the interface is represented by a surface grid moving with local velocities. It is obvious that this kind of method is

difficult to implement because it needs to deal with interaction between the two grids.

An alternative is to use indicator functions to distinguish different fluids in the flow field. In level set methods [6], the LS function represents a signed distance function which is positive on one fluid side and negative on the other side. The major drawback of the methods is lack of mass conservation, though the problem can be partially relieved by a reinitialization procedure [7,8].

VOF is another popular indicator function representing the fraction of one fluid occupying the control volume. Unlike other methods, conservation of mass can easily be attained in this approach. Among a variety of options, the one with interface reconstruction using a piecewise linear plane (PLIC) [9,10] is most favored. However, the reconstruction process and the calculation of flux across cell faces are complicated, especially serious in 3-D problems [11]. Unlike the LS function which is continuous, the VOF is a step function, i.e. discontinuous across the interface, which results in difficulties calculating geometric properties, such as interface normal or curvature. This leads to inaccurate calculation of the surface tension and, thus, unphysical spurious currents near the interface when the continuous surface force model (CSF) is incorporated in the VOF approach [12]. Several methods have been proposed to improve the estimation of surface tension and reduction of spurious currents. In the study of Francois et al. [13], a height function is reconstructed locally as an approximation of the interface location. The curvature is then estimated from this height function.

\* Corresponding author.

E-mail address: [yytsui@mail.nctu.edu.tw](mailto:yytsui@mail.nctu.edu.tw) (Y.-Y. Tsui).

## Nomenclature

$C$	specific heat	$\Delta v$	cell volume
$C_i$	volumetric flux through the $i$ th face	$We$	Weber number ( $= \rho_l V^2 d / \sigma$ )
$e$	specific energy	<b>Greek symbols</b>	
$Eo$	Eovots number ( $= \Delta \rho g d^2 / \sigma$ )	$\alpha$	VOF function
$\vec{f}_\sigma$	surface tension force	$\alpha^*$	smoothed VOF function
$\vec{g}, g$	gravitational acceleration	$\kappa$	mean curvature
$Gr$	Grashof number ( $= \rho_v \Delta \rho g \lambda^3 / \mu_v^2$ )	$\lambda$	characteristic length for film boiling
$h$	film thickness	$\lambda_d$	most dangerous Taylor wavelength
$h_{12}, h_{lv}$	latent heat of evaporation	$\mu$	viscosity
$Ja$	Jacob number ( $= C_v(T_w - T_{sat}) / h_{lv}$ )	$\rho$	density
$k$	thermal conductivity	$\Delta \rho$	density difference between the fluids
$\dot{m}$	mass flux	$\sigma$	surface tension
$Mo$	Morton number ( $= g \mu_l^4 / \rho_l \sigma^3$ )	$\vec{\tau}$	viscous stresses
$\vec{n}$	unit normal vector	<b>Subscripts</b>	
$\Delta n$	normal distance away from the interface	$C$	neighboring cell
$Nu$	Nusselt number	$f$	cell face
$\overline{Nu}$	space and time averaged Nusselt number	$ff$	$j$ th cell face
$Oh$	Ohnesorge number ( $= \mu_l / (\sigma \rho_l d)^{1/2}$ )	$int$	interface
$P$	pressure	$l$	liquid phase
$Pr$	Prandtl number ( $= C_v \mu_v / k_v$ )	$o$	octane
$Re$	Reynolds number ( $= \rho_l U d / \mu_l$ )	$P$	primary cell
$\dot{q}$	heat release rate	$sat$	saturation state
$\vec{s}_f$	surface vector of cell face	$v$	vapor phase
$\vec{s}_f^w$	surface vector of wetted area on cell face	$w$	water or wall value
$S_{int}$	interface surface in cell	$1, 2$	fluids 1 and 2
$S_M, S_x$	source terms in continuity and VOF equations	<b>Superscripts</b>	
$t$	time	$n$	new time step
$\Delta t$	time step size	$o$	old time step
$T$	temperature		
$\Delta T$	superheat temperature		
$U$	terminal velocity of rising bubble		
$V$	drop impact velocity		
$\vec{V}$	velocity vector		

In the PROST method of Renardy and Renardy [14], a least-squares fit of a quadratic surface to the VOF for each interface cell and its neighbors is calculated. Another option, which was developed by Sussman and Puckett [15] and gradually draws popularity recently, is to combine the advantages of both VOF and LS. This coupled LS and VOF method is achieved by advecting the interface using the conservative VOF function and estimating the interface normal and curvature using the continuous LS function. Modifications and applications of this CLSVOF method can be found in a number of studies [16–20].

Numerical analyses using the VOF and LS methods have been applied to various flow systems. Chen et al. [21] investigated the deformation of gas bubbles rising in a viscous liquid. The effects of density, Reynolds number, and surface tension on the formation of toroidal bubbles were examined. Another study on bubble rising was reported by Hua and Lou [22]. The comparison of simulations with experiments shows satisfactory agreement. Wide ranges of Reynolds number, Bond number, density ratio and viscosity ratio were under consideration. The study was extended by Hua et al. [23] to simulate fully 3-D bubble flows. Good agreement with experiments in terms of terminal speed and bubble shape was obtained. Also considered in this study is the interaction of two rising bubbles.

Boiling is an important thermal process due to its capability to convert large quantity of thermal energy from liquid to vapor phase. Son and coworkers conducted pioneer works to study bubble growth and release from a planar film [24] or a nucleate [25].

Esmaeli and Tryggvason [26] studied multi-mode film boiling on a plane sufficiently large to allow formation of bubbles of different sizes and spacings. Comparison of the overall mean Nusselt number with empirical correlation at different wall superheats showed reasonably good agreement. Film boiling on a horizontal cylinder was investigated by Son and Dhiri [27]. The effects of cylinder diameter and gravity on the flow and heat transfer were quantified. Tsui et al. [28] studied the effects of superheat on the bubble formation in planar film boiling. Five distinct regimes of bubble patterns were identified.

Temperature distribution during manufacturing process is crucial to the product quality of mold casting and injection molding processes. Modeling of the heat transfer in two-fluid flows without phase change has been made by Davidson and Rudman [29]. The heat transfer across the faces of the interface cell is obtained by considering the heat fluxes of individual fluids after the interface is reconstructed from the VOF distribution. In the study of Tsui et al. [30], satisfaction of the continuity condition for temperature and heat flux at the interface gives the interface temperature. This temperature is implemented as an internal Dirichlet condition for energy calculations.

As addressed above, the VOF-based PLIC method is popular among a variety of choices. In this method, the interface is rebuilt as a plane in the cell where the interface is located. The resulting interface is discontinuous across the common face shared by the neighboring cells. During the reconstruction process, iteration is usually required such that the wetted volume fraction in the cell

coincides with the local VOF value. This procedure is laborious and becomes very complicated in 3-D problems. In the newly developed approach CISIT, proposed by the present authors [31], the interface is simply represented by a contour surface corresponding to VOF value 0.5, which is easy to be constructed and continuous across the cells. Another difference between the two approaches is that to advance the interface in the former approach, integration over the interface is required to estimate the mass flux across each face of the cell. In our method, a predictor–corrector procedure is used, which is much easier to implement. In general, the CISIT method is robust and easy to implement. This method can easily be extended and applied to three-dimensional flows, as will be given in the following. Modeling of heat transfer across the interface for the 3-D flows with or without phase change is included. It is noted that in the calculations of the present study, the CSF approach is employed to model the surface tension in a similar way to that of Brackbill et al. [12]. The accuracy of the prediction can be improved by incorporating those methods like the height function method, the PROST, and the CLSVOF, as addressed above.

## 2. Mathematical formulation

The conservation laws to conserve the mass, momentum and energy for two different phases of a fluid or two immiscible fluids can be cast into one set of equations.

$$\nabla \cdot \vec{V} = S_M \quad (1)$$

$$\frac{\partial \rho \vec{V}}{\partial t} + \nabla \cdot (\rho \vec{V} \otimes \vec{V}) = -\nabla P + \nabla \cdot \tilde{\tau} + \rho \vec{g} + \vec{f}_\sigma \quad (2)$$

$$\frac{\partial \rho e}{\partial t} + \nabla \cdot (\rho \vec{V} e) = \nabla \cdot \left( \frac{k}{C} \nabla e \right) \quad (3)$$

The term  $\vec{f}_\sigma$  in the momentum equation, representing the surface tension force, is generally zero except in the cells containing the interface. The mass source  $S_M$  is non-zero when phase change takes place in the interface cells.

Within the frame of VOF methods, the interface is tracked by the volume fraction  $\alpha$  in the flow field. It is either zero or one in the single-fluid cells and falls between 0 and 1 in the cells containing the interface. The transport of this indicator function can be given by

$$\frac{\partial \alpha}{\partial t} + \nabla \cdot (\vec{V} \alpha) = S_\alpha \quad (4)$$

The source term is generally zero unless phase change occurs.

### 2.1. Smoothing

Since the mathematical problem becomes stiff due to the large variation of thermal properties across the interface, the density and viscosity used in the momentum equation are smoothed in the interface region as

$$\rho^* = \alpha^* \rho_1 + (1 - \alpha^*) \rho_2 \quad (5a)$$

$$\mu^* = \alpha^* \mu_1 + (1 - \alpha^*) \mu_2 \quad (5b)$$

where  $\alpha^*$  represents smoothed volume fraction. An averaging procedure is employed to smooth the function. First, the VOF value at each grid node is estimated by interpolation from the centroids of the cells sharing the node as a common vertex. It is followed that a new  $\alpha$  at each cell centroid is obtained by averaging over the surrounding vertices. In this way, the interface region is expanded on either side of the interface cell. Two such smoothing processes are undertaken to enhance smearing effects. It is noted that the thermal

properties in the energy equation are not smoothed. Special treatments will be given to enforce either the thermal jump or continuity condition, depending on whether phase change occurs, on the interface for calculating energy flux.

### 2.2. Surface tension model

The surface tension force can be evaluated by

$$\vec{f}_\sigma = \sigma \kappa \nabla \alpha^* \quad (6)$$

where  $\sigma$  is the surface tension. The curvature of the interface is calculated from

$$\kappa = \frac{1}{|\nabla \alpha^*|} \left[ \left( \frac{\nabla \alpha^*}{|\nabla \alpha^*|} \cdot \nabla \right) |\nabla \alpha^*| - \nabla \cdot \nabla \alpha^* \right] \quad (7)$$

### 2.3. Heat transfer model without phase change

Without phase change, both temperature and heat flux must be continuous at the contact surface between the two fluid flows.

$$T_{\text{int}} = T_1 = T_2 \quad (8)$$

$$\dot{q}_{\text{int}} = -k_1 \left( \frac{\partial T_1}{\partial n} \right) = -k_2 \left( \frac{\partial T_2}{\partial n} \right) \quad (9)$$

The temperature and heat flux at this contact surface can be determined from the two equations theoretically.

### 2.4. Heat and mass transfer model for phase change

With phase change, the temperatures of liquid and vapor at the interface are assumed to equal to the equilibrium saturation temperature corresponding to the system pressure. The jump of heat flux across the interface can be given as

$$\dot{q}_{\text{int}} = \dot{m}_{\text{int}} h_{12} = - \left( k \frac{\partial T}{\partial n} \right)_1 + \left( k \frac{\partial T}{\partial n} \right)_2 \quad (10)$$

where the subscripts 1 and 2 denote the liquid and the vapor states and  $h_{12}$  is the latent heat of evaporation. When the process of evaporation takes place, the mass transfer at the interface can be obtained by

$$\dot{m}_{\text{int}} = \rho_1 (\vec{V}_1 - \vec{V}_{\text{int}}) \cdot \vec{n} = \rho_2 (\vec{V}_2 - \vec{V}_{\text{int}}) \cdot \vec{n} \quad (11)$$

where  $\vec{n}$  denotes the unit vector normal to the interface. It can be rearranged to yield the normal flux of the vapor relative to the liquid.

$$(\vec{V}_2 - \vec{V}_1) \cdot \vec{n} = \left( \frac{1}{\rho_2} - \frac{1}{\rho_1} \right) \dot{m}_{\text{int}} \quad (12)$$

As seen from Eq. (10) that  $\dot{m}_{\text{int}} = \dot{q}_{\text{int}}/h_{12}$ , the mass production term on the right-hand side of the continuity equation (1) can then be given as

$$S_M = \frac{1}{\Delta v} \left( \frac{1}{\rho_2} - \frac{1}{\rho_1} \right) \int_{S_{\text{int}}} \frac{\dot{q}_{\text{int}}}{h_{12}} ds \quad (13)$$

where  $\Delta v$  is the volume of the considered cell and  $S_{\text{int}}$  denotes the phase surface within the cell. As for the VOF equation (4), its source term is given as

$$S_\alpha = \frac{1}{\Delta v} \left( -\frac{1}{\rho_1} \right) \int_{S_{\text{int}}} \frac{\dot{q}_{\text{int}}}{h_{12}} ds \quad (14)$$

It is noted that the heat generation rate  $\dot{q}_{\text{int}}$  can be determined from the jump of heat flux across the interface given in Eq. (10)

### 3. Numerical methods

In calculations, all variables are stored at the centroid of each cell. Discretization of the differential equations is carried out using a finite volume scheme [32]. To solve the Navier–Stokes equations, the convection flux at cell faces is approximated using the van Leer scheme arranged in a flux limiter form while the diffusion flux by an over-relaxed approach [33]. The coupling between momentum and continuity equations is tackled through an implicit treatment of the pressure gradients. Details of this approach are referred to the above references. The numerical methods related to the interface tracking and heat and mass transfers are described in the following.

#### 3.1. Tracking of the interface

In the CISIT method, the interface separating the two fluids is characterized by the contour surface of VOF value 0.5. To construct this surface, an interpolation procedure is employed. The VOF value is originally stored at the centroid of grid cell. An interpolation practice is first performed to find the VOF on grid nodes, which is obtained through a linear weighting using the VOF values of the cells sharing the node as a common vertex. It is followed by examining the two end nodes of each side edge which form the grid cell. The edge is intersected by the interface when the VOF value of one end node is less than 0.5 and the other greater than 0.5. For illustration, a 3-D grid cell is shown in Fig. 1. The interface cuts through three faces of the cell. The VOF less than 0.5 on vertices is designated by a solid circle while that greater 0.5 is denoted by a cross circle. The intersection point is located at the VOF value 0.5, obtained via linear interpolation from the two end nodes of the edge. In this way, a continuous piecewise linear interface can be built after this process proceeds throughout all the grid cells.

To advect the interface, conservation of the VOF in a cell, in which the interface is located, is considered. In Fig. 1, the surface vector of the cell face is denoted by  $\vec{s}_f$  and the part of the cell face wetted by one of the fluids by  $\vec{s}_f^w$ . The fluid flows into or out of the control volume through the wetted surfaces. Conservation of the fluid in this cell leads to

$$\frac{\Delta v_p}{\Delta t} (\alpha_p^n - \alpha_p^o) + \sum_j \vec{V}_{fj} \cdot \vec{s}_{fj}^w = -\frac{\dot{q}_{\text{int}}}{\rho_1 h_{12}} \Delta A_{\text{int}} \quad (15)$$

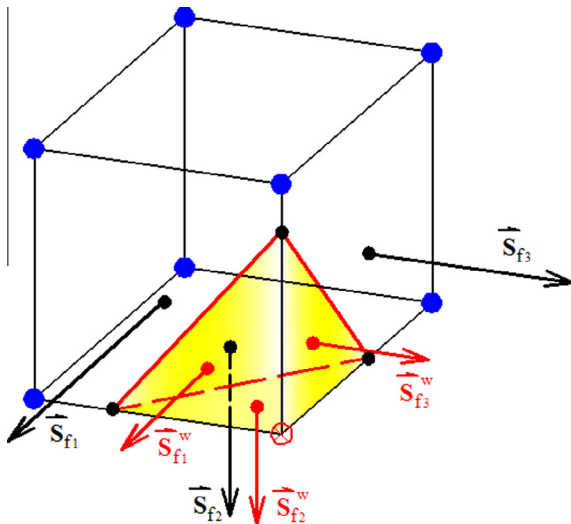


Fig. 1. A control volume partially filled by a fluid.

where  $\Delta A_{\text{int}}$  is the area of the interface embedded in the cell and the summation is over all the wetted faces. The term on the right side represents the amount of fluid change in the cell due to evaporation.

The above prediction procedure performs well if the interface remains in the cell during its motion in the time step. However, it cannot cope with the situation that the interface is moving out of or into a new cell in the time interval. The new VOF value may become greater than one or less than zero after solving Eq. (15). In the case  $\alpha_p > 1$  (overfilling), the cell is over filled by the fluid. To force the interface to move across the cell face, the excessive fluid  $\Delta\alpha (= \alpha_p - 1)$  must be portioned and reallocated to the downstream cells which surround the overfilling cell. The portioning factor  $w_i$  for a surrounding  $i$ -cell is based on the ratio of the efflux through the corresponding face to the total efflux.

$$w_i = \frac{\max(C_i, 0)}{\sum_j \max(C_j, 0)} \quad (16)$$

where  $C_i (= \vec{V}_{fi} \cdot \vec{s}_{fi})$  is the volumetric flux through the  $i$ th face and the sum is over all the faces. The VOF for the downstream cell is then corrected by

$$\alpha_i = \alpha_i + w_i(\alpha_p - 1) \frac{\Delta v_p}{\Delta v_i} \quad (17)$$

where  $\Delta v_i$  is the volume of the  $i$ -cell. After all the neighboring cells are adjusted, the VOF value  $\alpha_p$  of the overfilling cell is reset to 1.

The fluid is over depleted in the cell as  $\alpha_p < 0$  (overdepleting). The overdepleted volume of fluid must be retrieved from the neighboring, downstream cells. Similar to the overfilling case, the portioning factor can be calculated from Eq. (16). The VOFs of the neighboring cells are adjusted as

$$\alpha_i = \alpha_i + w_i \alpha_p \frac{\Delta v_p}{\Delta v_i} \quad (18)$$

It is followed by assigning a zero value to  $\alpha_p$ .

There is a possibility that, different from the overfilling,  $\alpha_p$  may become less than 1 (underfilling) when the interface advances to leave the cell in high shear flows. This situation can be checked to find that the VOFs on all the vertices of the cell are greater than 0.5. Since the interface does not exist in this cell any more, the VOF will remain unchanged in calculations. To remedy this problem, fluid must be retrieved from the downstream cells to refill this cell such that  $\alpha_p$  is equal to 1. The adjustment process is similar to that given in the overfilling case.

Another possibility in strong shear flows is that  $\alpha_p$  may remain greater than 0 (underdepleting) as the interface retreats from the cell, i.e. the VOFs on all the vertices of the cell become less than 0.5. Similar to the underfilling, the fluid will remain in this cell in calculations. To correct this situation, the residue fluid in this cell must be allocated to the downstream cells such that  $\alpha_p$  becomes zero, similar to that in the overdepleting case.

After one sweep of such corrections, some neighboring cells may become over filled or over depleted. Hence, two correction steps are undertaken to ensure no overshoots and undershoots in the VOF field.

#### 3.2. Treatments of heat transfer across the interface

Unlike the PLIC method, in which the interface is approximated by a flat plane in the cell, the interface is represented by a piecewise linear plane in the present method. As shown in Fig. 2, the interface can be composed of 1 to 4 triangular planes provided that only one interface appears in the cell. It is needed to estimate the heat flux through each individual triangle for the total heat transfer across the interface in the cell.

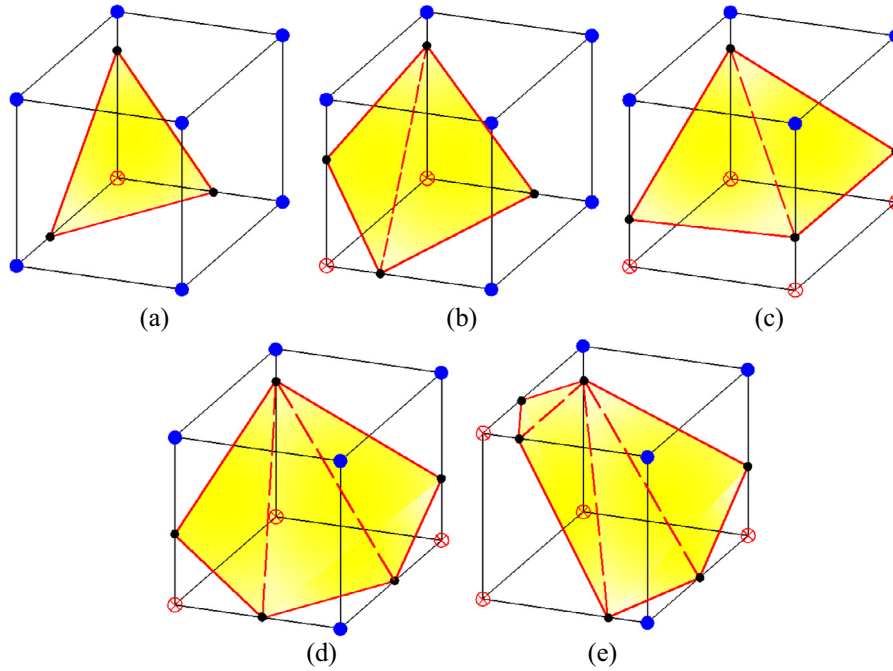


Fig. 2. Five types of interface cells (solid circle vertex:  $\alpha < 0.5$ ; cross circle vertex:  $\alpha > 0.5$ ).

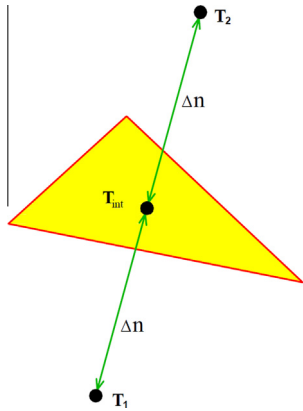


Fig. 3. Illustration of heat flux calculation on a triangular interface.

The temperature gradients are not continuous when approaching the interface from either side. Therefore, it is better to approximate the gradients using one-sided difference. As an illustration, a triangular plane is shown in Fig. 3. The heat fluxes on both sides of the plane are approximated by

$$\dot{q}_1 = -k_1 \frac{T_{\text{int}} - T_1}{\Delta n}, \quad \dot{q}_2 = -k_2 \frac{T_2 - T_{\text{int}}}{\Delta n} \quad (19)$$

The temperatures  $T_1$  and  $T_2$  at nodes 1 and 2 are obtained using interpolation from the surrounding temperatures. The normal distance  $\Delta n$  is chosen as 1.5 times the grid size. For the problem without phase change, the heat flux is continuous at the interface, i.e.  $\dot{q}_1 = \dot{q}_2$ . With this condition, the interface temperature can be derived to give

$$T_{\text{int}} = \frac{k_1 T_1 + k_2 T_2}{k_1 + k_2} \quad (20)$$

In the problems with phase change,  $T_{\text{int}}$  is fixed as the saturation temperature at the system pressure. The total heat flux is obtained by taking sum over all the triangular surfaces.

$$\dot{q}_{\text{int}} \Delta A_{\text{int}} = \sum_i \dot{q}_{\text{int}}^i \Delta A_{\text{int}}^i \quad (21)$$

### 3.3. Implementation of heat flux condition at the interface

The interface can be regarded as an internal boundary with Neumann conditions imposed on it. In order to solve the temperature fields for the two fluids as one, special treatments are required. For the cells adjacent to the interface cell to see proper heat flux, an approximation is practiced to find the temperature at the centroid of the interface cell or on the face of this cell.

It is assumed that only one interface is present in the cell. It is possible to have more than one interface in a cell. However, the process to handle this kind of cell will become extremely complicated. We simply ignore these cells in calculations. Fortunately, this situation is hardly encountered in our test cases. Five generic types of interface configurations are shown in Fig. 2. No treatment is necessary for the cell shown in Fig. 2(e) because the interface appears in all the neighboring cells. The temperature at the cell centroid needs to be estimated for the cell types (a), (b) and (d). Different from the above, the interface cuts across the four side faces in Fig. 2(c). For this type, the temperatures at both the centroid and the cell face on the other fluid side (i.e. the top or bottom face, depending on whether the interface is above or below the centroid) are required. To illustrate the calculation procedure, this cell is reproduced in Fig. 4. First, the mean normal vector and the mean temperature gradient are calculated.

$$\vec{n} = \frac{\vec{n}^1 \Delta A^1 + \vec{n}^2 \Delta A^2}{\Delta A^1 + \Delta A^2} \quad (22)$$

$$\frac{\partial T}{\partial n} = \frac{(\frac{\partial T}{\partial n})^1 \Delta A^1 + (\frac{\partial T}{\partial n})^2 \Delta A^2}{\Delta A^1 + \Delta A^2} \quad (23)$$

The superscripts 1 and 2 denote the two interface planes. The mean temperature gradients on the two fluid sides need to be estimated separately. Based on the mean normal vector, a plane surface is constructed as shown in Fig. 4(b). Then, the temperatures at the centroid and the face on the opposite side are calculated by



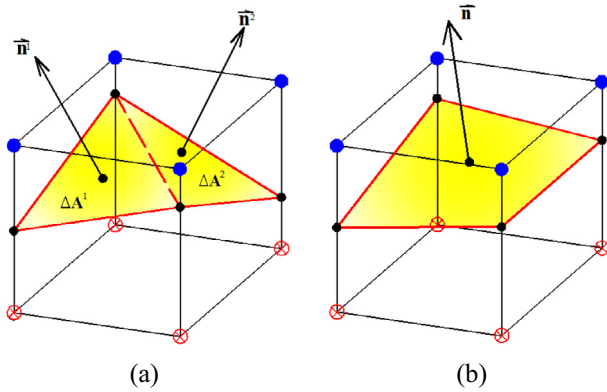


Fig. 4. Calculation of heat flux for the interface type (c) in Fig. 2.

$$T_p = T_{\text{int}} + \left( \frac{\partial T}{\partial n} \right)_1 \Delta n_p \quad (24)$$

$$T_f = T_{\text{int}} + \left( \frac{\partial T}{\partial n} \right)_2 \Delta n_f \quad (25)$$

where  $\Delta n_p$  and  $\Delta n_f$  are the normal distances from the interface to the centroid and the face, respectively. These temperatures form a Dirichlet boundary condition for the adjacent non-interface cells. In solving the energy equation, the discretized equation is expressed as

$$A_p T_p = \sum A_c T_c + S \quad (26)$$

where the subscript  $C$  denotes the surrounding cells. In order to fix the temperature  $T_p$  in the interface cell obtained above, the following settings are specified.

$$A_p = D, \quad A_c = 0, \quad S = D T_p \quad (27)$$

where  $D$  is a great number.

#### 4. Results and discussion

To assess the solution method, we first consider the deformation of a fluid sphere in a prescribed flow field. It is then applied to realistic flows, including the bubble flow rising in quiescent water and the splashing of a drop impacting on a thin liquid film. The modeling of phase change is validated by examining the formation of a boiling bubble emerging from a planar film. The heat transfer model is tested in a flow resulting from injection of high-temperature octane into water.

##### 4.1. Deformation of a sphere in prescribed velocity field

In this test, a sphere of fluid is deformed by a velocity field given by [34]

$$u = 2 \sin^2(\pi x) \sin(2\pi y) \sin(2\pi z) \cos\left(\frac{\pi t}{T}\right) \quad (28a)$$

$$v = -\sin(2\pi x) \sin^2(\pi y) \sin(2\pi z) \cos\left(\frac{\pi t}{T}\right) \quad (28b)$$

$$w = -\sin(2\pi x) \sin(2\pi y) \sin^2(\pi z) \cos\left(\frac{\pi t}{T}\right) \quad (28c)$$

where  $T = 3$  is the time period. The domain size is  $(1, 1, 1)$ . The sphere radius is 0.15 and centered on  $(0.35, 0.35, 0.35)$  initially. In

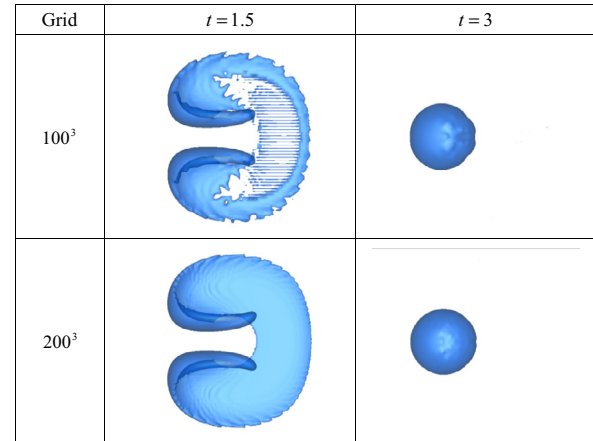


Fig. 5. Deformation of the sphere at  $t = 1.5$  and  $3.0$  for two different grids.

the first half of a time period, the sphere is deformed by the shear flow. The flow is reversed in the second half period. The deformed sphere is recovered during this time and finally returns to its original shape by the end of the period.

Fig. 5 presents the results for  $100^3$  and  $200^3$  grids at  $t = 1.5$  and  $3.0$ , corresponding to the times of maximum deformation and full recovery. It can be seen that the fluid body is deformed significantly and the tail part become very thin at  $t = 1.5$ . The lower resolution of the coarse grid results in fragmentation of the body. With increase of the grid density, no fragmentation is found and the original spherical shape is almost recovered by the end of the period. Table 1 shows  $L_1$  errors and convergence rates at  $t = 3.0$ . The error decreases with the increase of grid density. The convergence rate of the method is around 1.8, close to 2.

##### 4.2. Rising of a bubble

The rising of bubble in liquids is one of the most common two-phase phenomena. Grace [35] has analyzed a large body of experimental data on bubble shapes and terminal velocities and came to a diagram in which three dimensionless parameters are related: Eovots number ( $Eo = \Delta \rho g d^2 / \sigma$ ), Morton number or Bond number ( $Mo = g \mu_l^4 / \rho_l \sigma^3$ ), and Reynolds number ( $Re = \rho_l U d / \mu_l$ ), in which  $d$  is the effective diameter of the bubble and  $U$  is the terminal velocity of the rising. In simulations, the initial diameter of the bubble is  $d = 0.01$  m and the water tank is in the size  $5d \times 5d \times 5d$ . Only a quarter of the domain is considered in calculations, which is partitioned into  $25 \times 25 \times 150$ ,  $50 \times 50 \times 300$  and  $75 \times 75 \times 450$  control volumes. Symmetrical condition is assumed on the side boundaries.

Three cases are under test, corresponding to  $(Eo = 1, Mo = 10^{-3})$ ,  $(Eo = 10, Mo = 1)$ , and  $(Eo = 100, Mo = 10^3)$ . The first case is located in the spherical regime in the Grace diagram. As the surface tension is reduced by one order, the second case falls on the edge between the spherical and ellipsoidal regimes. Further decrease of the surface tension by one more order, the third case is on the margin of the dimpled cap regime. The predicted bubble shapes at the terminal velocities are shown in Fig. 6. It can be seen that these shapes are consistent with those indicated in the Grace diagram, especially by using fine grids. However, a significant difference

Table 1  
 $L_1$  errors and convergence rates for the deformation test case.

Grid	$L_1$ error	Convergence rate
$50^3$	$4.20 \times 10^{-3}$	–
$100^3$	$1.18 \times 10^{-3}$	1.83
$200^3$	$3.48 \times 10^{-4}$	1.76

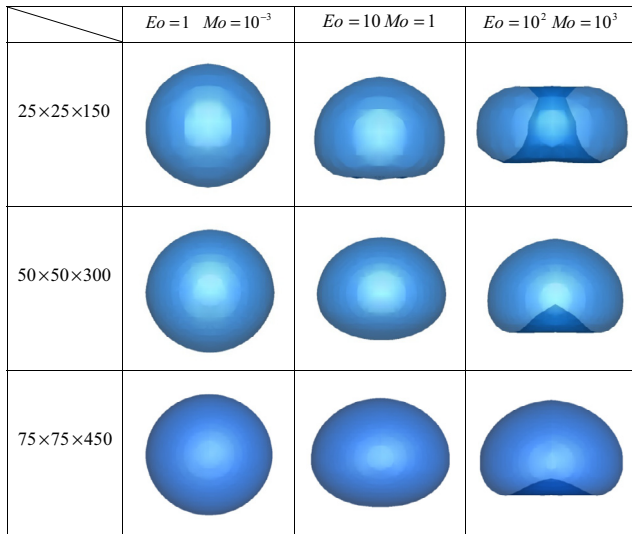


Fig. 6. Bubble shapes for the considered cases using different grids.

Table 2

Reynolds numbers at terminal velocity for the rising bubble case.

	25 × 25 × 150	50 × 50 × 300	75 × 75 × 450
$Eo = 1, Mo = 10^{-3}$	$Re = 4.58$	$Re = 4.04$	$Re = 3.92$
$Eo = 10, Mo = 1$	$Re = 3.69$	$Re = 3.42$	$Re = 3.32$
$Eo = 10^2, Mo = 10^3$	$Re = 2.34$	$Re = 3.15$	$Re = 2.99$

can be observed in the third case when using different grids. With the lowest grid resolution, a toroidal bubble is formed whereas the bubble is in the shape of a cap with a dimple at the lower surface for fine grids. The formation of a toroidal bubble is due to lack of grid resolution and also appears in the study of Bonometti and Magnaudet [36]. The computed Reynolds numbers based on the terminal velocity are presented in Table 2. The Reynolds number slightly decreases as the dimensionless numbers increase due to the deviation of the bubble shape away from spherical geometry. When the grid is refined, the Reynolds number becomes smaller. The Reynolds number for the coarsest grid is the lowest in the third case, which is a direct result of the formation of the toroidal shape.

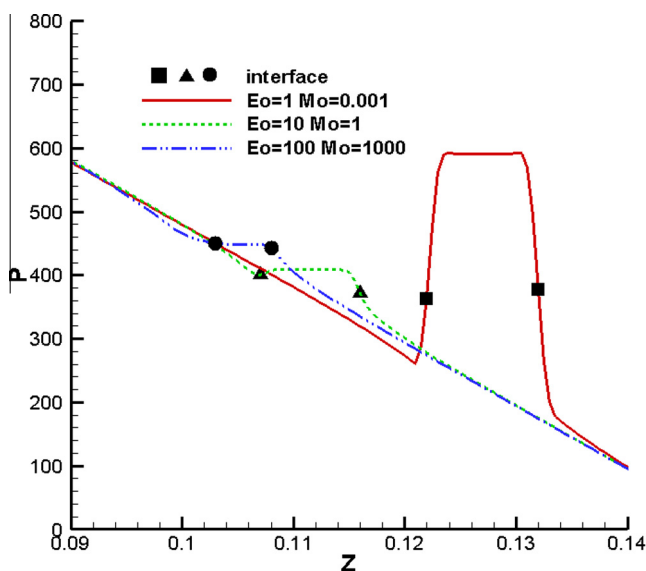


Fig. 7. Variation of pressure along the vertical axis at the tank center.

With the finest grid, the Reynolds number is 2.99 for the third case, comparable to the Grace's correlation of around 2. The difference may be attributed to the uncertainty of the correlation.

The pressure distribution along the vertical axis at the center, obtained by using the second finest grid, is shown in Fig. 7. The positions of the phase surface are marked in the curves. It is clear that the pressure in the core of the bubble is fairly uniform. The pressure outside the bubble varies in a nearly linear sense, closely related to the hydrostatic pressure. It is worth to notice that the smaller surface tensions in cases 2 and 3 lead to lower pressure gradients at the phase surface and, thus, lower pressure levels inside the bubble. Careful examination of the curves reveals that different from cases 1 and 2, the pressure gradient at the lower interface in case 3 becomes negative, i.e. the pressure inside the bubble is lower than that outside. This explains the cause of the dimple on the lower surface.

As seen above, the portrait of the bubble for the first case is very close to a sphere. According to the Young–Laplace equation, the pressure jump across a spherical surface is  $\Delta p = 2\sigma/r$ , giving a pressure difference  $392 \text{ N/m}^2$  for the bubble with a radius  $0.005 \text{ m}$ . The pressure difference between the bubble center and that outside the bubble at the same vertical position as the center in the first case is  $376 \text{ N/m}^2$ .

#### 4.3. Splash of a drop

The impact of a drop on a liquid film has attracted attention of scientists for a long time [37]. The dimensionless parameters relevant to this subject are Weber number ( $We = \rho_l V^2 d / \sigma$ ), Ohnesorge number ( $Oh = \mu_l / (\sigma \rho_l d)^{1/2}$ ), and dimensionless film thickness ( $H = h/d$ ). It is assumed in the following calculation that  $We = 400$ ,  $Oh = 0.0016$ , and  $H = 0.1$ . The diameter  $d$  of the drop is  $0.005 \text{ m}$  and the impact velocity  $V$  is  $0.25 \text{ m/s}$ . The size of the computational domain is  $6d \times 6d \times 3d$ . Only a quarter of the domain, covered by a  $210 \times 210 \times 210$  grid, is considered in calculations.

The temporal evolution of the splashing process is shown in Fig. 8. Immediately after impact of the drop on the thin film a ring wave is formed, as seen at  $t = 1 \text{ ms}$ . The wave propagates radially outward to form a crown-like sheet at  $t = 2 \text{ ms}$ . A free rim can be detected at the top of the crown. It is followed that the sheet under

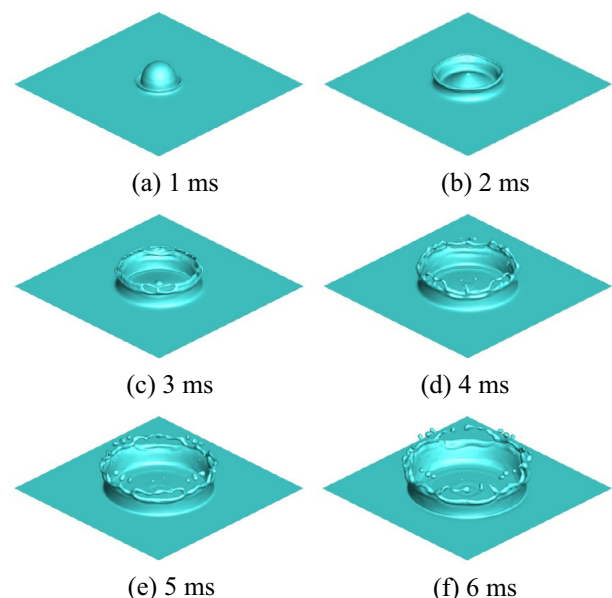


Fig. 8. Splashing dynamics of a drop impacting on a thin film.

the rim is broken. As time reaches 4 ms, secondary droplets are formed due to capillary breakup. More droplets are found at later times. The above process of wave propagation, transformation to crown sheet, and formation of droplets is better illustrated on the symmetric plane given in Fig. 9. The radial propagation of the crown can be characterized by its radius. A correlation was proposed by Rieber and Frohn [38].

$$\frac{r_c}{d} = 6H^{-1/4}T^{1/2} \quad (29)$$

where  $T (=tV/d)$  is the dimensionless time. It is seen from Fig. 10 that the agreement of the predictions with the correlation is reasonably good.

#### 4.4. Film boiling

The boiling system is assumed to be saturated at 1 atm and 227 °C. The thermal properties are given in the following, which

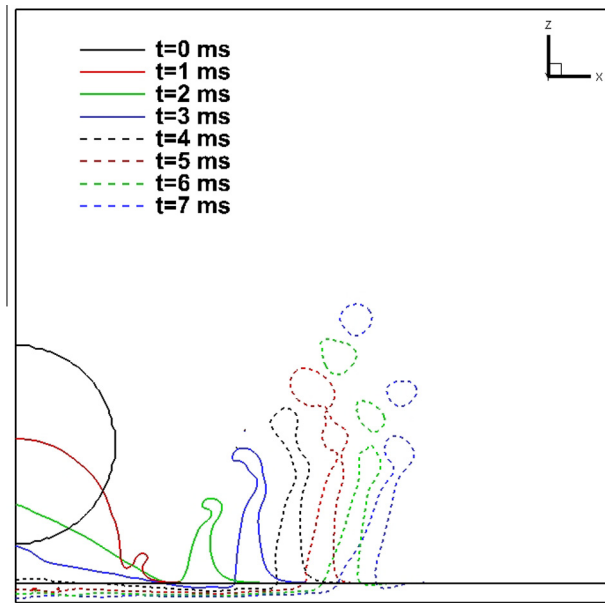


Fig. 9. Evolution of the ring wave on a symmetric plane.

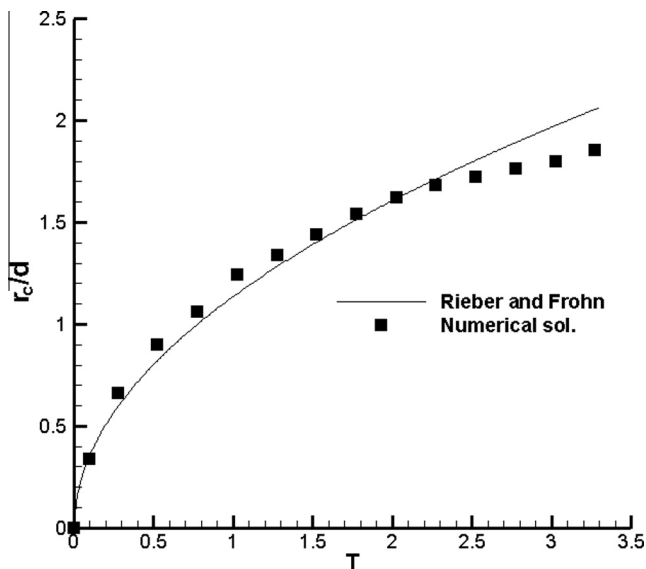


Fig. 10. Temporal variation of the crown sheet front.

were used by Welch and Wilson [39] in their 2-D boiling flow simulation.

$$\rho_v = 5 \text{ kg/m}^3, \quad \mu_v = 0.005 \text{ Pa} \cdot \text{s}, \quad k_v = 1 \text{ W/(m} \cdot \text{K)}, \\ C_v = 0.2 \text{ kJ/kg} \cdot \text{K}$$

$$\rho_l = 200 \text{ kg/m}^3, \quad \mu_l = 0.1 \text{ Pa} \cdot \text{s}, \quad k_l = 40 \text{ W/(m} \cdot \text{K)}, \\ C_l = 0.4 \text{ kJ/kg} \cdot \text{K}$$

The latent heat is  $h_{lv} = 10 \text{ kJ/kg}$  and the surface tension  $\sigma = 0.1 \text{ N/m}$ . The characteristic length, defined as  $\lambda = \sqrt{\sigma/(\rho_l - \rho_v)g}$ , is  $0.00723 \text{ m}$ . The 2-D most dangerous Taylor wavelength is  $\lambda_d = 2\sqrt{3}\pi\lambda = 0.08 \text{ m}$ . The computational domain is  $\lambda_d \times \lambda_d \times 2\lambda_d$  and  $100 \times 100 \times 200$  grid is used in computation. A superheated vapor film is placed beneath a bulk of saturated water. The initial film is perturbed with a peak at the film center.

$$z = \frac{\lambda_d}{8} + \frac{\lambda_d}{64} \left[ \cos\left(\frac{2\pi(x - \lambda_d/2)}{\lambda_d}\right) + 1 \right] \left[ \cos\left(\frac{2\pi(y - \lambda_d/2)}{\lambda_d}\right) + 1 \right] \quad (30)$$

The bottom wall is fixed at certain superheated temperatures. The initial temperature in the film is assumed to vary linearly from the wall to the saturated liquid. The top boundary is open while symmetry condition is imposed on the side boundaries.

A Nusselt number averaged over the bottom wall is defined by

$$Nu = \frac{1}{A} \int_0^{\lambda_d} \int_0^{\lambda_d} \frac{\lambda}{(T_w - T_{sat})} \frac{\partial T}{\partial n} \bigg|_w dx dy \quad (31)$$

where  $A$  is the area of the wall. The time variation of this Nusselt number for superheat  $\Delta T = 10^\circ \text{C}$  is shown in Fig. 11. It is obvious that it approaches a periodic variation with period around  $0.29 \text{ s}$  after  $t = 1.0 \text{ s}$ . The dynamics of the boiling process is illustrated in Fig. 12. At  $t = 1.0 \text{ s}$ , a bubble is found to be ready to detach. It is noticed that the film is quite thin and nearly flat at the edges at this instant. The bubble breaks off from the film later at  $t = 1.03 \text{ s}$ . It can be identified that a dimple is formed at the film center, resulted from the pulling force of the surface tension after the bubble pinches off. This reflects that a capillary wave is formed and propagates radially outward. The evaporation process continues to transform more liquid into vapor, resulting in increase of the film thickness. Vapor is gathered in the central region of each film edge

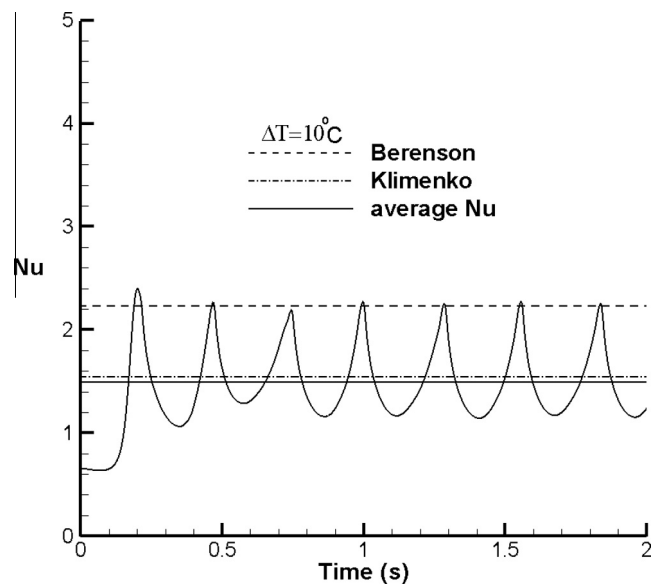


Fig. 11. Variation of the Nusselt number for the film boiling.



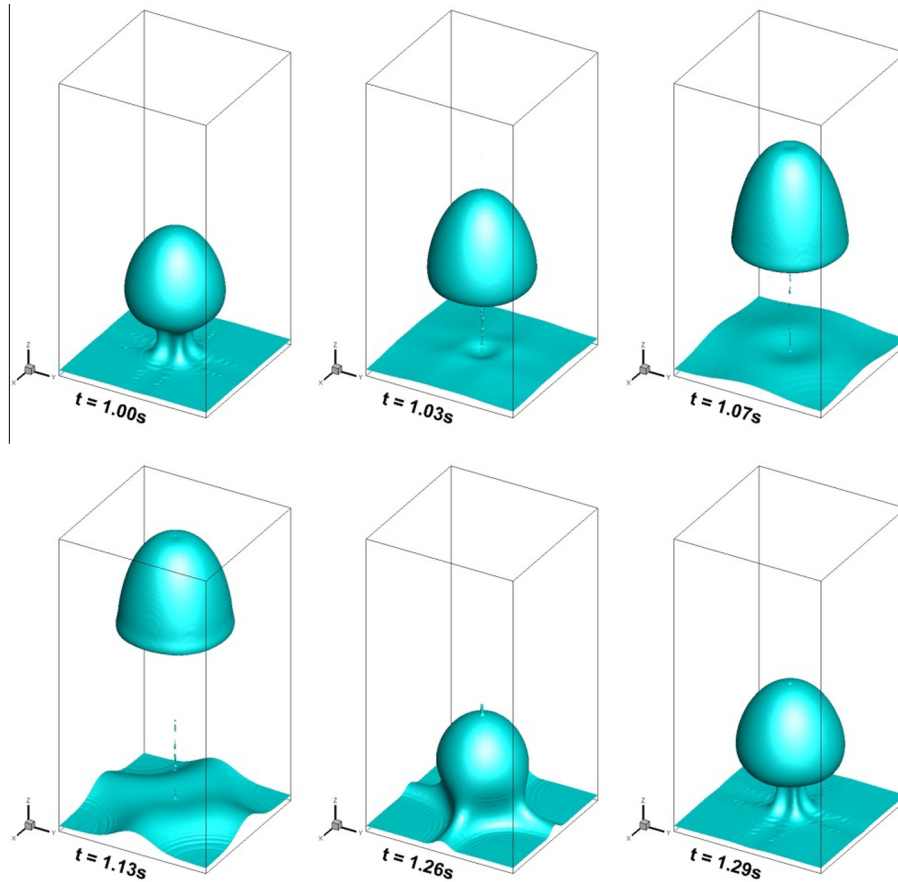


Fig. 12. Bubble growth and release in the film boiling process.

to form a hump there. The film thickness reaches a maximum at  $t = 1.13$  s. It is followed by flowing of vapor towards the film center to form a bubble, which causes diminishing of the thickness at the outskirts of the film. The process completes a cycle when time reaches  $t = 1.29$  s.

Fig. 13 presents temperature contours on a vertical plane. It can be detected that the temperature varies nearly in a linear manner from  $T_w$  at the bottom wall to  $T_{sat}$  at the phase surface. Since the heat transfer is inversely proportional to the film thickness, it is not unexpected to find a maximum of  $Nu$  at  $t = 1.0$  s and a minimum at 1.13 s. in Fig. 11. The capillary wave can be identified from the temperature contours at  $t = 1.03$  and 1.13 s.

Averaging the Nusselt number over the entire computational time gives a value 1.50, which is shown in Fig. 11. Also seen in the figure are the correlations of Berenson [40] and Klimenko [41]. The empirical correlation of Berenson's model is given by

$$Nu_B = 0.425[Gr \times Pr/Ja]^{1/4} \quad (32)$$

Here  $Gr$  is the Grashof number,  $Pr$  the Prandtl number and  $Ja$  the Jacob number. Klimenko's model can be applied up to turbulent regime.

$$Nu_K = \begin{cases} 0.19Gr^{1/3}Pr^{1/3}f_1, & \text{for } Gr \leq 4.03 \times 10^5 \\ 0.0216Gr^{1/2}Pr^{1/3}f_2, & \text{otherwise} \end{cases} \quad (33)$$

where  $f_1$  and  $f_2$  are correction factors depending on  $Ja$ . It can be seen from Fig. 11 that the time-averaged  $Nu$  is lower than the two correlations, but with a very close agreement with Berenson's model. More comparisons of predictions with the models are shown in Fig. 14. At lower superheats of  $\Delta T = 7.5$  and  $5^\circ\text{C}$ , the time-averaged  $Nu$  becomes higher (1.53 and 1.60, respectively).

This trend is also seen in the models. However, the increase of the predictions is not so large as the models.

#### 4.5. Injection of octane into water tank

In this case, we apply the interfacial heat transfer model to a high-temperature octane flow injected into a tank full of water. The octane, at  $80^\circ\text{C}$ , emerges from an orifice of diameter 1 mm located at the bottom of a cylindrical container  $30 \times 6$  mm in size. The water temperature in the tank is initially  $20^\circ\text{C}$ . The inlet flow is assumed to be fully developed with a maximum speed 1 m/s at the center. In simulation, only a quarter of the cylinder is under consideration, which is subdivided into 2187599 cells. The thermal properties of the octane and water are listed below.

$$\rho_o = 660.32 \text{ kg/m}^3, \quad \mu_o = 4 \times 10^{-4} \text{ Pa} \cdot \text{s}, \\ k_o = 0.12 \text{ W/(m} \cdot \text{K)}, \quad C_o = 2.278 \text{ kJ/kg} \cdot \text{K}$$

$$\rho_w = 995 \text{ kg/m}^3, \quad \mu_w = 5.5 \times 10^{-4} \text{ Pa} \cdot \text{s}, \\ k_w = 0.643 \text{ W/(m} \cdot \text{K)}, \quad C_w = 4.217 \text{ kJ/kg} \cdot \text{K}$$

The surface tension is  $\sigma = 0.043 \text{ N/m}$ .

A jet is formed as the octane flows out of the orifice. Instability is triggered on the surface between the two fluids due to amplification of small disturbances. The instability is then magnified to cause breakup of the jet to form droplets. In the study of liquid jet into a stagnant gas, four main breakup regimes have been identified [42]: namely Rayleigh breakup mode, first wind-induced mode (or wavy breakup mode), second wind-induced mode, and atomization mode. The cause of the different modes is due to the effects of different combinations of liquid inertia, surface tension,

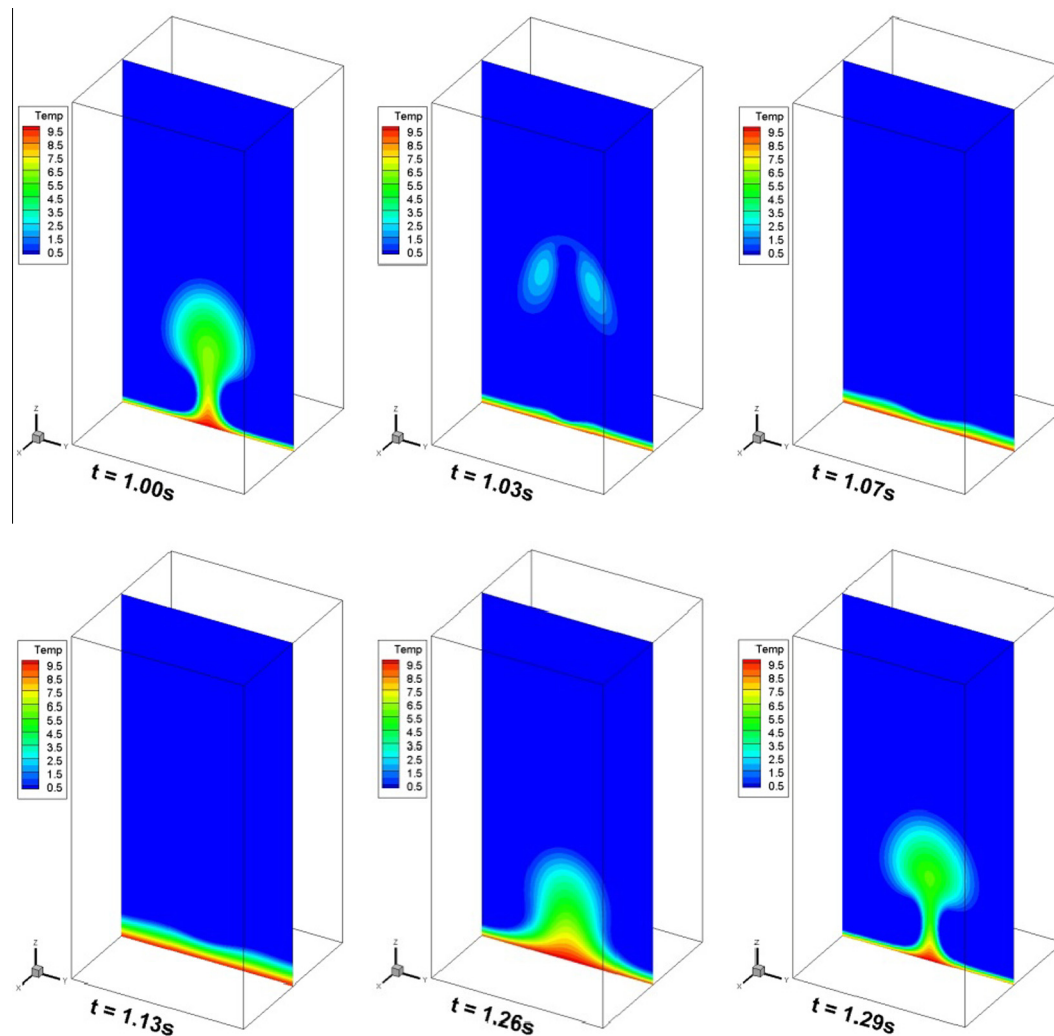


Fig. 13. Temperature distribution on a vertical plane in the film boiling flow.

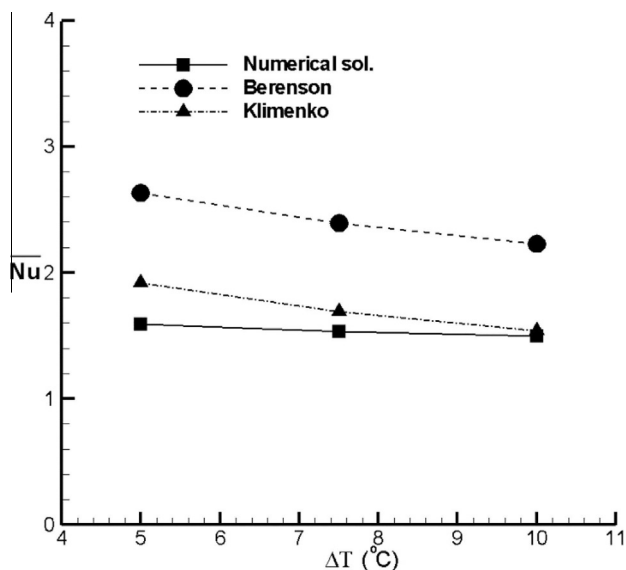


Fig. 14. Variation of mean Nusselt number with superheats.

and fluid dynamic forces acting on the jet. It is essential to identify these forces to explain the breakup mechanism in each mode.

At low velocities in the Rayleigh breakup regime, perturbations are amplified by the surface tension, which propagates as a surface wave. Amplification of this capillary instability leads to breakup of the jet into droplets in the size larger than the jet diameter. As flow velocity increases, a shear appears at the interface. Aerodynamic forces become important and must be taken into account. The jet breakup is resulted from the coupled effects of the capillary instability and the Kelvin–Helmholtz instability, typical of shear flows, in this wavy breakup regime. The size of produced droplets is on the same order of the jet diameter. Further increase of jet velocity leads to second wind-induced mode. The flow becomes turbulent and the breakup occurs at the vicinity of the nozzle. At ultimate velocities, atomization mode is reached and droplets are found at the nozzle exit. The droplet size is much less than the jet diameter in the second wind-induced and atomization regimes.

It is clear from Fig. 15 that the flow is in the Rayleigh and wavy breakup regimes evidenced by the fact that the resulted drops after breakup are on the same order of the jet size. As addressed above, both the surface tension and shear stress play important roles during the breakup. At  $t = 0.03$  s, a neck is formed at the middle height of the jet while a spherical head is seen at the top end. It is followed by disintegration of the jet at  $t = 0.04$  s. By  $t = 0.08$  s, three

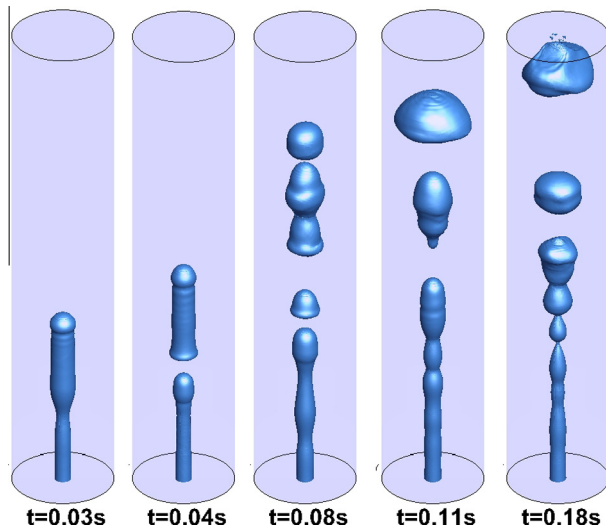


Fig. 15. The breakup process of the octane injection flow.

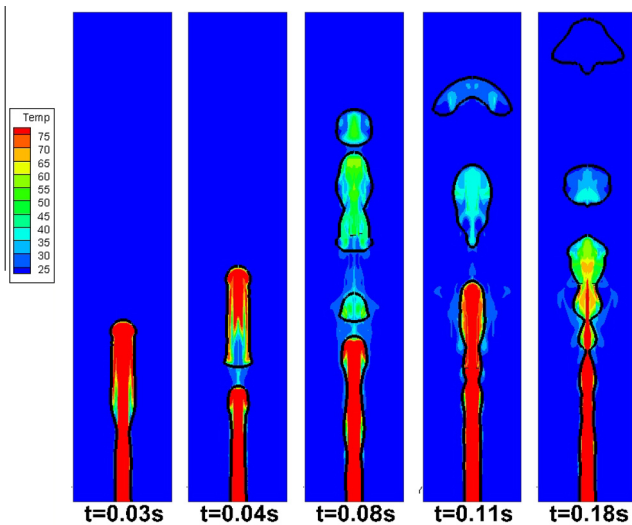


Fig. 16. Temperature distribution in the octane injection flow.

fragments are found. When time proceeds to  $t = 0.11$  s, the surface tension brings about a cap-shape drop at the top of the tank. It can be seen that at  $t = 0.18$  s, the wavy surface is going to pinch off to form a number of drops. The corresponding temperature distribution is shown in Fig. 16. The temperature in the jet maintain at high levels before it breaks off. The temperature in the fragments declines quickly due to the disconnection with the thermal source of the jet.

## 5. Conclusions

The VOF based CISIT method has been extended to deal with three-dimensional flow problems. In this approach, the interface is rebuilt as a contour surface which is continuous across the cells. The advection of the interface is realized by a predictor–corrector procedure. There is no need to know detailed geometry of the reconstructed interface in the CISIT method. Only the wetted areas on the cell faces are required. Tests on rising bubbles show that fairly good agreement with Grace diagram is obtained in terms of bubble shape and terminal velocity. It is seen from the simula-

tion results for the drop impact on a liquid film that the splashing processes characterized by ring wave propagation, formation of a crown sheet, and detachment of droplets are well reproduced. To calculate the heat flux at the interface in heat transfer problems, the reconstructed surface is assumed to be made of triangular planes. For the film boiling flow the mechanism to cause cyclic formation of discrete bubble is clearly delineated. Reasonably good agreement with available correlations is obtained. In the last case, the injection of octane into a tank results in formation a jet. The breakup of the jet to form drops due to the capillary wave is clearly seen in the simulation.

## Conflict of interest

None declared.

## Acknowledgments

This work was supported by the National Science Council of R.O.C. under the Contract Number NSC 102-2221-E009-059 and by the Ministry of Science and Technology of R.O.C. under the Contract Number MOST 103-2221-E009-072.

## References

- [1] O. Ubbink, R.I. Issa, A method for capturing sharp fluid interfaces on arbitrary meshes, *J. Comput. Phys.* 153 (1999) 26–50.
- [2] Y.-Y. Tsui, S.-W. Lin, T.-T. Cheng, T.-C. Wu, Flux-blending schemes for interface capture in two-fluid flows, *Int. J. Heat Mass Transfer* 52 (2009) 5547–5556.
- [3] D. Juric, G. Tryggvason, Computations of boiling flows, *Int. J. Multiphase Flow* 24 (1998) 387–410.
- [4] G. Tryggvason, B. Bunner, A. Esmaeili, D. Juric, N. Al-Rawahi, W. Tauber, J. Han, S. Nas, Y.-J. Jan, A front-tracking method for the computations of multiphase flow, *J. Comput. Phys.* 169 (2001) 708–759.
- [5] S. Shin, D. Juric, Modeling three-dimensional multiphase flow using a level contour reconstruction method for front tracking without connectivity, *J. Comput. Phys.* 180 (2002) 427–470.
- [6] S. Osher, R.P. Fedkiw, Level set methods: an overview and some recent results, *J. Comput. Phys.* 169 (2001) 463–502.
- [7] M. Sussman, P. Smereka, S. Osher, A level set approach for computing solutions to incompressible two-phase flow, *J. Comput. Phys.* 114 (1994) 146–159.
- [8] M. Sussman, E. Fatami, P. Smereka, S. Osher, An improved level set method for incompressible two-phase flows, *Comput. Fluids* 27 (1998) 663–680.
- [9] W.J. Rider, D.B. Kothe, Reconstructing volume tracking, *J. Comput. Phys.* 141 (1998) 112–152.
- [10] J.E. Pilliod Jr., E.G. Puckett, Second-order accurate volume-of-fluid algorithms for tracking material interfaces, *J. Comput. Phys.* 199 (2004) 465–502.
- [11] C.S. Wu, D.L. Young, H.C. Wu, Simulations of multidimensional interfacial flows by an improved volume-of-fluid method, *Int. J. Heat Mass Transfer* 60 (2013) 739–755.
- [12] J.U. Brackbill, D.B. Kothe, C. Zemach, A continuum method for modeling surface tension, *J. Comput. Phys.* 100 (1992) 335–354.
- [13] M.M. Francois, S.J. Cummins, E.D. Dendy, D.B. Kothe, J.M. Sicilian, M.W. Williams, A balanced-force algorithm for continuous and sharp interfacial surface tension models within a volume tracking framework, *J. Comput. Phys.* 213 (2006) 141–173.
- [14] Y. Renardy, M. Renardy, PROST: a parabolic reconstruction of surface tension for the volume-of-fluid method, *J. Comput. Phys.* 183 (2002) 400–421.
- [15] M. Sussman, E.G. Puckett, A coupled level set and volume-of-fluid method for computing 3D and axisymmetric incompressible two-phase flows, *J. Comput. Phys.* 162 (2000) 301–337.
- [16] G. Son, N. Hur, A coupled level set and volume-of-fluid method for the buoyancy-driven motion of fluid particles, *Numer. Heat Transfer, Part B: Fundam.* 42 (2002) 523–542.
- [17] G. Tomar, G. Biswas, A. Sharma, A. Agrawal, Numerical simulation of bubble growth in film boiling using a coupled level-set and volume-of-fluid method, *Phys. Fluids* 17 (2005) 112103.
- [18] A. Albadawi, D.B. Donoghue, A.J. Robinson, D.B. Murray, Y.M.C. Delaure, Influence of surface tension implementation in volume of fluid and coupled volume of fluid with level set methods for bubble growth and detachment, *Int. J. Multiphase Flow* 53 (2013) 11–28.
- [19] I. Chakraborty, G. Biswas, P.S. Ghoshdastidar, A coupled level-set and volume-of fluid method for the buoyant rise of gas bubbles in liquids, *Int. J. Heat Mass Transfer* 58 (2013) 240–259.
- [20] B.M. Ningegowda, B. Premachandran, A coupled level set and volume of fluid method with multi-directional advection algorithms for two-phase flows with and without phase change, *Int. J. Heat Mass Transfer* 79 (2014) 532–550.

- [21] L. Chen, S.V. Garimella, J.A. Reizes, E. Leonard, The development of a bubble rising in a viscous liquid, *J. Fluid Mech.* 387 (1999) 61–96.
- [22] J. Hua, J. Lou, Numerical simulation of bubble rising in viscous liquid, *J. Comput. Phys.* 222 (2007) 769–795.
- [23] J. Hua, J.F. Stene, P. Lin, Numerical simulation of 3D bubbles rising in viscous liquids using a front tracking method, *J. Comput. Phys.* 227 (2008) 3358–3382.
- [24] G. Son, V.K. Dhir, Numerical simulation of film boiling near critical pressures with a level set method, *ASME J. Heat Transfer* 120 (1998) 183–192.
- [25] G. Son, V.K. Dhir, N. Ramanujapu, Dynamics and heat transfer associated with a single bubble during nucleate boiling on a horizontal surface, *ASME J. Heat Transfer* 121 (1999) 623–631.
- [26] A. Esmaeli, G. Tryggvason, Computations of film boiling part II: multi-mode film boiling, *Int. J. Heat Mass Transfer* 47 (2004) 5463–5476.
- [27] G. Son, V.K. Dhir, Three-dimensional simulation of saturated film boiling on a horizontal cylinder, *Int. J. Heat Mass Transfer* 51 (2008) 1156–1167.
- [28] Y.-Y. Tsui, S.-W. Lin, Y.-N. Lai, F.-C. Wu, Phase change calculations for film boiling flows, *Int. J. Heat Mass Transfer* 70 (2014) 745–757.
- [29] M.R. Davidson, M. Rudman, Volume-of-fluid calculation of heat or mass transfer across deforming interfaces in two-fluid flow, *Numer. Heat Transfer, Part B: Fundam.* 41 (2002) 291–308.
- [30] Y.-Y. Tsui, S.-W. Lin, K.-J. Ding, Modeling of heat transfer across the interface in two-fluid flows, *Numer. Heat Transfer, Part B: Fundam.* 66 (2014) 162–180.
- [31] Y.-Y. Tsui, S.-W. Lin, A VOF based conservative interpolation scheme for interface tracking (CISIT) of two-fluid flows, *Numer. Heat Transfer, Part B: Fundam.* 63 (2013) 263–283.
- [32] Y.-Y. Tsui, Y.-F. Pan, A pressure-correction method for incompressible flows using unstructured meshes, *Numer. Heat Transfer, Part B: Fundam.* 49 (2006) 43–65.
- [33] Y.-Y. Tsui, T.-C. Wu, A pressure-based unstructured-grid algorithm using high resolution schemes for all-speed flows, *Numer. Heat Transfer, Part B: Fundam.* 53 (2008) 75–96.
- [34] R. LeVeque, High-resolution conservative algorithms for advection in incompressible flow, *SIAM J. Numer. Anal.* 33 (1996) 627–665.
- [35] J.R. Grace, Shape and velocities of bubbles rising in infinite liquids, *Trans. Inst. Chem. Eng.* 51 (1973) 116–120.
- [36] T. Bonometti, J. Magnaudet, Transition from spherical cap to toroidal bubbles, *Phys. Fluids* 18 (2006) 052102.
- [37] A.L. Yarin, Drop impact dynamics: splashing, spreading, receding, bouncing... , *Annu. Rev. Fluid Mech.* 38 (2006) 159–192.
- [38] M. Rieber, A. Frohn, A numerical study on the mechanism of splashing, *Int. J. Heat Fluid Flow* 20 (1999) 455–461.
- [39] S.W.J. Welch, J. Wilson, A volume of fluid based method for fluid flows with phase change, *J. Comput. Phys.* 160 (2000) 662–682.
- [40] P.J. Berenson, Film-boiling heat transfer from a horizontal surface, *ASME J. Heat Transfer* 83 (1961) 351–358.
- [41] V.V. Klimenko, Film-boiling on a horizontal plate – New correlation, *Int. J. Heat Mass Transfer* 24 (1981) 69–79.
- [42] S.P. Lin, R.D. Reitz, Drop and spray formation from a liquid jet, *Annu. Rev. Fluid Mech.* 30 (1998) 85–105.